Electronic Sensor and Actuator Webs for Large-Area Complex Geometry Cardiac Mapping and Therapy

Dae-Hyeong Kim[1⊥], Roozbeh Ghaffari[2⊥], Nanshu Lu[3⊥], Shuodao Wang[4⊥], Stephen P. Lee[2], Hohyun Keum[5], Robert D'Angelo[2], Lauren Klinker[2], Yewang Su[4], Chaofeng Lu[4,6], Yun-Soung Kim[5], Abid Ameen[5], Yuhang Li[4,7], Yihui Zhang[4], Bassel de Graff[2], Yung-Yu Hsu[2], Zhuangjian Liu[8], Jeremy Ruskin[9], Lizhi Xu[5], Chi Lu[5], Fiorenzo G. Omenetto[10], Yonggang Huang[4], Moussa Mansour[9], Marvin J. Slepian[11], John A. Rogers[5*]

[1]*Center for Nanoparticle Research of Institute for Basic Science, School of Chemical and Biological Engineering, WCU Program of Chemical Convergence for Energy and Environment, Seoul National University, Seoul 151-742, Republic of Korea*

[2]*MC10 Inc., 36 Cameron Avenue, Cambridge, MA 02140 USA*

[3]*Department of Aerospace Engineering and Engineering Mechanics, University of Texas at Austin, Austin, TX 78712, USA*

[4]*Department of Mechanical Engineering and Department of Civil and Environmental Engineering, Northwestern University, Evanston, IL 60208*

[5]*Department of Materials Science and Engineering, Beckman Institute for Advanced Science and Technology, and Frederick Seitz Materials Research Laboratory, University of Illinois at Urbana-Champaign, Urbana, IL 61801 USA*

[6]*Soft Matter Research Center & Department of Civil Engineering, Zhejiang University, Hangzhou 310058, China*

[7]*School of Astronautics, Harbin Institute of Technology, Harbin 150001, China*

[8]*Institute of High Performance Computing, 1 Fusionopolis Way, #16-16 Connexis, Singapore 138632.*

[9]*Massachusetts General Hospital, Cardiac Arrhythmia Unit, Boston, MA. 02140 USA*

[10]*Department of Biomedical Engineering, Tufts University, Medford, MA. 02155 USA*

[11]*Sarver Heart Center, University of Arizona, Tucson, AZ 85724 USA*

[⊥]*These authors contributed equally.*

*To whom correspondence should be addressed. E-mail: jrogers@illinois.edu

Supporting Information

1. SI Materials and Methods

Fabrication of the EGM webs

The fabrication starts with spin coating of polyimide (PI, ~1.2 μm, Sigma Aldrich, USA) onto a film of poly(methylmethacrylate) (PMMA, 100 nm, MicroChem, USA) cast on a silicon wafer. Electron beam evaporation forms an adhesion layer and metallization for island and interconnects (Cr/Au, 5 nm/150 nm), defined into appropriate patterns by photolithography and etching. A second, top layer of PI (~1.2 μm) insulates the system and places the metal near the neutral mechanical plane in the PI/metal/PI stack. The open web design results from etching through the entire thickness of this trilayer with oxygen reactive ion etching (RIE) in a pattern defined by photolithography. The final device appears in Fig. 1*A*. The total number of paired electrodes is 17. Dissolving the silk substrate releases a free-standing web that is transfer printed to a silk substrate, and then connected to an anisotropic conductive film (ACF) for interfacing to a data acquisition system, thereby completing the fabrication.

Fabrication of temperature sensor and strain gauge webs

The designs and fabrication procedures are similar to those described above. The temperature sensing web uses platinum resistors at the locations of the islands. Here, thin layers of Ti/Pt (5 nm/50 nm) deposited by electron beam evaporation and patterned by

photolithography and then lift-off defines the sensors. Surface treatment of the PI with UV/Ozone or deposition of a thin silicon dioxide (SiO_2) layer (~50 nm) on top of PI improves the adhesion of the Ti/Pt. Fabrication of strain gauge rosettes relies on transfer printing of boron-doped (doping concentration ~ 5×10^{18} /cm^3), 340nm-thick silicon resistors onto the island regions. Both sensors use serpentine interconnects of Cr/Au. Additional encapsulation with PI prevents electrical leakage currents, and places the components near the neutral mechanical plane. A final device appears in Fig. 1*A*. Transfer printing the mesh to silk and establishing ACF connections completes the process. The temperature sensor and strain gauge arrays contain 16 and 8 paired nodes, respectively. Detailed designs of temperature sensor and strain gauge array appear in Fig. S3 and S7, respectively.

Fabrication of impedance contact sensor webs and integration on collapsible balloon catheters

The fabrication process is identical to the stretchable electrode array processing, but with the addition of an encapsulating layer of polymer (Dymax Inc.) for planarization (Fig. S10). Flexible printed circuit boards connect to the sensor arrays using anisotropic conductive epoxy, applied with heat (175° C) and pressure. Thin-walled heat shrink tubing insulates the ribbons and wires, to provide water-proof encapsulation.

Impedance-based contact, temperature and strain gauge data acquisition design

The data acquisition system consists of three modules to measure impedance-based contact, temperature and strain (Fig. S11). A MMBT4403 PNP transistor is placed in the

feedback path of the AD8671 operational amplifier to create a voltage-controlled current source. For contact sensing, the excitation current from the current source passes through tissue to generate a voltage, which is then measured with a National Instruments PXI-6289 data acquisition card. Custom LabView software was written to control the output current and frequency of the excitation current. The excitation currents were set <10 μA and measurements were collected at 1 kHz and 10 kHz. For temperature and strain gauge recordings, two custom, multi-channel software-controlled current sources operate the web arrays. A PXI-6289, controlled with custom LabView software, controls voltages across either sensor type. The excitation consisted of a DC current between 50 μA to 1 mA.

Electrophysiological signal data acquisition design

The electrophysiological signals detected by the web arrays were conditioned with an Intan RHA1016 multiplexed biopotential amplifier. A digital signal processing system (Grapevine system, Ripple Inc) converted the multiplexed analog signal from the RHA1016 to digital output. The RHA1016's output was sampled at 300 ksps and decimated at 1 ksps for individual channels. In addition, the Grapevine system applied a digital 50/60 Hz notch filter to the signal. The data are recorded in the Cyberkinetics NEV2.2 NS2 format and viewed with custom Matlab software.

Animal preparations

Experiments used rabbit models (n = 5; 3.5-4.0 kg), anaesthetized with a 0.5 ml/kg mixture of ketamine (30 mg/kg), xylazine (7 mg/kg) and acepromazine (3:5 mg/kg), and then intubated and maintained with 2% isoflurane at room temperature. Access to the

epicardial surface is enabled by sternotomy and pericardiotomy. Once exposed, sensor webs placed in direct contact with the anterior surface of the ventricles provides the measurement modality. Ringer's solution maintains a moist epicardial surface during experiments. Measurements made at multiple sites along RV and LV surfaces allow differentiation of local excitation across the different chambers of the heart during normal and following ischaemic-injury.

Porcine models (n = 3; 80-100 kg) were anesthetized. Heart rate monitoring electrodes, EGM, respiratory rate, intravenous blood pressure monitor and a periodic toe pinch to test for pedal withdrawal provided assessment of anesthetic depth. Lactated Ringer's solution was administered via IV at a rate of 10 mL/kg/hr (Saline 0.9% solution 10mL/kg/hr can be substituted). Jugular and femoral venous access were achieved by shaving the skin around these areas to facilitate access in the veins. The guide-wires, cardiac sheaths, were deployed via the femoral vein. Contrast dye was injected into the balloon and x-ray images were captured to determine the position of the balloon during inflation cycles. The Institutional Animal Care and Use Committee at the University of Arizona approved of all experiments.

2. Detailed information of the electrical system and temperature sensor

The size of one electrode (see Fig. S1) is 560 μm × 290 μm and the center to center distance between electrodes in one differential pair is 1 mm. When films of chromium (5 nm; adhesion promoter) / gold (150 nm), deposited by electron beam evaporation and

photolithographically patterned into pads with dimensions of 250 μm × 250 μm are used, the impedance is ~84 kOhm (measured in saline solution using the integrated device structure, with interconnects and the sensing electrode exposed). Typically the electrical impedance reduces to ~29 kOhm with the addition of a bilayer titanium (5 nm; adhesion promoter) / platinum (50 nm) on top of the same chromium / gold electrode. The signal to noise ratios estimated directly from recorded EGM signals measured when mounted on the epicardial surface are typically greater than 40 (with gold electrodes). The center-to-center distance between each electrode pair is more than ~3 mm, which is sufficiently large to minimize cross-talk. The entire electrode array in the current design measures ~16 mm × ~14 mm and can cover the exposed surfaces of hearts in small animal models. Straightforward scaling of the same fabrication schemes, materials and mechanics designs can enable analogous devices for the human heart. One of the advantages of cardiac web design is, as described in the frictional analysis, that it minimizes effects of sliding, thereby suppressing motion artifacts. The criterion for acceptable leakage current was less than ~10 μA, typically less than ~1 μA.

Precision hot plates were used to establish calibration curves for the temperature sensors. After establishing conformal contact of a sensor to the center of the hot plate, the resistance change was measured as a function of temperature. The time response associated with changes in resistance is less than a second. The normalized (resistance of each measurement divided by the resistance at the initial temperature) calibration results and non-normalized, raw results appear in Fig. 2*D* and its inset. The resistance varies linearly

with temperature, as expected. Depending on the detection electronics, the precision of the temperature measurement can be as high as ~0.02°C.

3. Tensile and Bending stiffness of mapping electrode arrays

The electrode arrays (Fig. 1*A*) consist of electrode islands of widths w_x and w_y, double serpentine interconnects along the *y*- direction (Figs. S2*A* and *C*) and single serpentine interconnects along the *x*-direction (Fig. S2*B*) with arc radii *r* and *R* and width *b*. The interconnects are much more compliant than the electrode islands such that they deform to accommodate all stretching and/or bending. The tensile and bending stiffness of mapping electrode arrays, with and without the silk substrate, are obtained analytically in the following.

For an interconnect subjected to a pair of forces *F* at both ends, the bending moment *M* in the interconnect is obtained in terms of coordinates of the center of cross location, and is linearly proportional to *F*. The strain energy is dominated by the bending energy, which is given by $U \approx U_{\text{bending}} = \int M^2 ds \Big/ \left(2\overline{EI}_{z,\text{int}}\right)$, where $\overline{EI}_{z,\text{int}}$ is the in-plane bending stiffness of the interconnect, and the integration is along the arc length *s* of the interconnect. The elongation of each interconnect is $u = \partial U / \partial F$, which is linearly proportional to *F*. The effective tensile stiffness of the electrode arrays without the silk substrate is

$$\begin{cases} \overline{EA}_x = \dfrac{F\left(w_x + L_{bx}\right)}{u\left(w_y + L_{by}\right)} \\ \overline{EA}_y = \dfrac{2F\left(w_y + L_{by}\right)}{u\left(w_x + L_{bx}\right)} \end{cases}, \tag{S1}$$

where $L_{by}=2R+8r$ and $L_{bx}=2R+4r$ are bridge lengths along y- and x- directions in Figs. S2*A* and S2*B*, respectively. Equation (S1) can also be written analytically as

$$\begin{cases} \overline{EA}_x = \dfrac{\overline{EI}_{z,\text{int}}\left(w_x + 2R + 4r\right)}{2R^3\left(w_y + 2R + 8r\right)} \left\{ \begin{array}{l} \dfrac{3}{4}\pi - \dfrac{5}{3} + \pi\eta + 4\eta^2 + \dfrac{\pi}{2}\eta^3 \\ -\dfrac{\left[\pi - 3 + 2\left(\pi - 2\right)\eta + 2\pi\eta^2 + 4\eta^3\right]^2}{3\pi - 8 + 8\left(\pi - 2\right)\eta + 8\pi\eta^2 + 6\pi\eta^3} \end{array} \right\}^{-1} \\ \overline{EA}_y = \dfrac{\overline{EI}_{z,\text{int}}\left(w_y + 2R + 8r\right)}{R^3\left(w_x + 2R + 4r\right)} \left\{ \begin{array}{l} \dfrac{3}{4}\pi - 1 + 2\pi\eta + 8\eta^2 + \pi\eta^3 \\ -\dfrac{\left(1+2\eta\right)^2\left[\pi - 3 + 2\left(\pi - 1\right)\eta + 4\eta^2\right]^2}{3\pi - 8 + 16\left(\pi - 2\right)\eta + 32\left(\pi + 1\right)\eta^2 + 44\pi\eta^3} \end{array} \right\}^{-1} \end{cases}, \tag{S2}$$

where $\eta=r/R$. The tensile stiffness of electrode arrays with the silk substrate is given by

$$\begin{cases} \overline{EA}_{x\text{-silk}} = \overline{EA}_x + \overline{E}_{\text{silk}} h_{\text{silk}} \\ \overline{EA}_{y\text{-silk}} = \overline{EA}_y + \overline{E}_{\text{silk}} h_{\text{silk}} \end{cases}, \tag{S3}$$

where $\overline{E}_{\text{silk}}$ and h_{silk} are the elastic modulus and thickness of silk substrate, respectively.

For an interconnect subjected to a pair of out-of-plane bending moments M_0 at both ends, the bending moments in the normal direction M_n, out-of-plane direction M_z and torque T_s in the interconnect is obtained in terms of the orientation of the cross section, and is linearly proportional to M_0. The strain energy is dominated by the bending and torsion energies, and is given by

$$U \approx U_{\text{bending-}n} + U_{\text{bending-z}} + U_{\text{torsion}} = \int M_n^2 ds \Big/ \left(2\overline{EI}_{n,\text{int}}\right) + \int M_z^2 ds \Big/ \left(2\overline{EI}_{z,\text{int}}\right) + \int T_s^2 ds \Big/ \left(2\overline{GJ}_s\right) \quad ,$$

where $\overline{EI}_{n,\text{int}}$ is the bending stiffness in the *n*-direction (Figs. S2*A* and S2*B*), and $\overline{GJ}_s$ is the torsion stiffness of the interconnect. The relative rotation between two ends of the interconnect is $\theta_0 = \partial U / \partial M_0$, which is linearly proportional to M_0. The effective bending stiffness of the electrode arrays without the silk substrate is

$$\begin{cases} \overline{EI}_x = \dfrac{M_0\left(w_x + L_{bx}\right)}{\theta_0\left(w_y + L_{by}\right)} \\ \overline{EI}_y = \dfrac{2M_0\left(w_y + L_{by}\right)}{\theta_0\left(w_x + L_{bx}\right)} \end{cases}, \tag{S4}$$

or

$$\begin{cases} \overline{EI}_x = \dfrac{2\overline{GJ}_s\left(w_x + 2R + 4r\right)}{R\left(w_y + 2R + 8r\right)}\left[\begin{matrix} 4 + \pi + 2\pi\eta + \pi\beta\left(1 + 2\eta\right) \\ -\dfrac{4\left(\beta - 1\right)^2}{\beta\left(4 + \pi + 2\pi\eta\right) + \pi\left(1 + 2\eta\right)} \end{matrix}\right]^{-1} \\ \overline{EI}_y = \dfrac{4\overline{GJ}_s\left(w_y + 2R + 8r\right)}{R\left(w_x + 2R + 4r\right)}\left[\begin{matrix} 12 + \pi + 4\pi\eta + \pi\beta\left(1 + 4\eta\right) \\ -\dfrac{4\left(\beta - 1\right)^2}{\beta\left(12 + \pi + 4\pi\eta\right) + \pi\left(1 + 4\eta\right)} \end{matrix}\right]^{-1} \end{cases}, \tag{S5}$$

where $\beta = \overline{GJ}_s / \overline{EI}_{n,\text{int}}$. The bending stiffness of the electrode arrays with the silk substrate can be similarly obtained following the approach by Kim *et al.* (1) and Wang *et al.* (2). These analytical expressions of the tensile and bending stiffness agree very well with FEA, as shown in the Table S1 and 2.

The stiffness along the *x* and *y* directions are, in fact, quite similar such that only their average values are reported in the paper. The analysis above does not account for

buckling of the interconnects, which would result in even smaller tensile/bending stiffness such that the electrode arrays in experiments may be more compliant than the above results.

4. Coupling between the electrode array and the epicardial surface

The total potential energy $U_{\text{non-couple}}=0$ when the electrode array has no contact with the epicardial surface and remains flat. Once the electrode array conforms to the epicardial surface, the total energy U_{couple} consists of the elastic energy $U_{\text{elastic}} = U_{\text{bending}} + U_{\text{membrane}} = L^2 \overline{EI}_{\text{mesh}} / R_{\text{heart}}^2 + \pi \overline{EA}_{\text{mesh}} \int_0^{L/\sqrt{\pi}} \left[1 - R_{\text{heart}} \sin\left(r/R_{\text{heart}}\right)/r\right] r dr$ and the adhesive energy of the interface $U_{\text{adhesive}} = -\gamma A$. Intimate coupling between the electrode array and the epicardial surface requires $U_{\text{couple}} = U_{\text{elastic}} + U_{\text{adhesive}} < U_{\text{non-couple}} = 0$, which leads to Eq. (1).

The interfacial bonding between rigid ribbons and a deforming substrate (the expanding/contracting heart in this case) is well studied by Lu et al. (3) who give the energy release rate for stiff ribbons on compliant substrate (E_{heart}<<E_{device}) analytically as $G_{\text{ribbon}} = \frac{E_{\text{heart}} \varepsilon^2 L_{\text{unit}}}{8} \tan \frac{\pi w_x}{2L_{\text{unit}}}$. In the current study, however, only part of the area (w_y/L_{unit}) is bonded to the electrode islands, and therefore the energy release rate is multiplied by this area ratio and given approximately as Eq. (2) in the text.

5. Equilibrium between the electrode island, the interconnects and the epicardial tissue

Let F_x and F_y denote the forces acting on an electrode island along the *x*- and *y*-directions (Fig. S2*F*, grey rectangular denotes the island; red substrate denotes the heart, modelled as a semi-infinite body, with *z*-direction pointing into the heart), respectively. The forces F_x and F_y are uniformly distributed over the area of the island $w_x \times w_y$. As a result, the displacements of the island at point *O* under these forces are derived from the Mindlin solution as (4)

$$\begin{aligned}\Delta_{\text{island}-x} &= \frac{1+\nu}{\pi E_{\text{heart}}}\frac{F_x}{w_x w_y}\int_{-w_y/2}^{w_y/2}\int_{-w_x/2}^{w_x/2}\left[\frac{1-\nu}{\sqrt{X^2+Y^2}}+\frac{\nu X^2}{\left(X^2+Y^2\right)^{3/2}}\right]dXdY \\ &= \frac{(1+\nu)F_x}{\pi w_x E_{\text{heart}}}\left[\ln\left(\frac{\sqrt{1+a^2}+1}{\sqrt{1+a^2}-1}\right)+\frac{1-\nu}{a}\ln\left(\frac{\sqrt{1+a^2}+a}{\sqrt{1+a^2}-a}\right)\right]\end{aligned} \tag{S6}$$

and

$$\begin{aligned}\Delta_{\text{island}-y} &= \frac{1+\nu}{\pi E_{\text{heart}}}\frac{F_y}{w_x w_y}\int_{-w_y/2}^{w_y/2}\int_{-w_x/2}^{w_x/2}\left[\frac{1-\nu}{\sqrt{X^2+Y^2}}+\frac{\nu Y^2}{\left(X^2+Y^2\right)^{3/2}}\right]dXdY \\ &= \frac{(1+\nu)F_y}{\pi w_y E_{\text{heart}}}\left[\ln\left(\frac{\sqrt{1+a^2}+a}{\sqrt{1+a^2}-a}\right)+(1-\nu)a\ln\left(\frac{\sqrt{1+a^2}+1}{\sqrt{1+a^2}-1}\right)\right]\end{aligned} \tag{S7}$$

in the *x*- and *y*- directions, respectively, where $a=w_y/w_x$. The interconnects are subjected to the same forces and therefore elongate. The elongations of the interconnects are

$$\Delta_{\text{int}-x} = \frac{F_x}{\overline{EA}_{\text{mesh}}} \tag{S8}$$

in the *x*-direction and

$$\Delta_{\text{int}-y} = \frac{F_y}{\overline{EA}_{\text{mesh}}} \tag{S9}$$

in the *y*-direction. If there is no slippage between the islands and the heart, then

$$\Delta_{\text{island}-x} + \Delta_{\text{int}-x} = \Delta_{\text{island}-y} + \Delta_{\text{int}-y} = \varepsilon L_{\text{unit}} . \tag{S10}$$

The total pulling force at each electrode island is $F_{\text{pull}} = \sqrt{F_x^2 + F_y^2}$. Substituting Eq. (S6-S10) into the above expression yields $F_{\text{pull}} = \overline{EA}_{\text{mesh}} \varepsilon L_{\text{unit}} g_1 \left(\frac{\overline{EA}_{\text{mesh}}}{E_{\text{heart}} w_x}, \frac{w_y}{w_x}, \frac{w_x}{L_{\text{unit}}}, \nu \right)$, where

$$g_1 = \sqrt{\begin{aligned} &\left\{ 1 + \frac{(1+\nu)\overline{EA}_{\text{mesh}}}{\pi w_x E_{\text{heart}}} \left[\ln\left(\frac{\sqrt{1+a^2}+1}{\sqrt{1+a^2}-1} \right) + \frac{1-\nu}{a} \ln\left(\frac{\sqrt{1+a^2}+a}{\sqrt{1+a^2}-a} \right) \right] \right\}^{-2} \\ &+ \left\{ 1 + \frac{(1+\nu)\overline{EA}_{\text{mesh}}}{\pi w_y E_{\text{heart}}} \left[\ln\left(\frac{\sqrt{1+a^2}+a}{\sqrt{1+a^2}-a} \right) + (1-\nu) a \ln\left(\frac{\sqrt{1+a^2}+1}{\sqrt{1+a^2}-1} \right) \right] \right\}^{-2} \end{aligned}} . \tag{S11}$$

6. Friction coefficient between the electrode array and the epicardial tissue

Patronik *et al.* (5) reported a frictional force of f~3 N in studies of epicardial surface on which a small robot was mounted over an area of A~35 mm^2 by suction at vacuum pressure of p~53 kPa. The friction coefficient is thus obtained as $\mu = f/(pA) \sim 1.6$. Other friction studies have reported smaller friction coefficient (e.g., 0.04~0.2 (6)), but even for the friction coefficient to be an order of magnitude smaller, Eq.

(3) still holds such that the electrode array does not slide because buckling of interconnects gives much smaller pulling force on the electrode island.

7. Thermal analysis of heart during cryoablation

For cryoablation to a specific region in the heart, the heat conduction equation for the temperature T is

$$k\nabla^2 T = \frac{k}{\alpha}\frac{\partial T}{\partial t}, \tag{S17}$$

where k and α are the thermal conductivity and diffusivity of heart tissue, respectively, and t is time. The ventricular wall of the heart is modeled as a slab of thickness $h = 1.9$ mm, with the initial temperature 37 ^{o}C (body temperature). The dry ice is approximately a cylinder with radius ~ 3.5 mm and much larger height. The outer surface of the ventricular wall in contact with the dry ice and the air temperature around the dry ice are the sublimation temperature -79 ^{o}C of dry ice (7), which governs the natural heat convection with the outer surface of the ventricular wall. The inner surface of the ventricular wall has heat convection with the blood of constant temperature 37 ^{o}C, but the convection coefficient is low when the ventricular wall contacts the dry ice (and therefore low temperature and slow blood flow (8)). Once the dry ice is removed, the outer surface of the ventricular wall has natural heat convection with the room-temperature air. The inner surface has heat convection with the blood flow at constant temperature of 37 ^{o}C, though the convection coefficient increases substantially (8) for relatively fast blood flow.

The heat conduction equation is solved numerically. Its spatial and temporal distributions are shown in Figs. 2*F* and S5*B*, respectively, and the latter agrees well with experiments.

8. Thermal analysis of heart during RF ablation

For RF ablation of a specific region in the heart, the heat conduction equation is

$$k\nabla^2 T + q = \frac{k}{\alpha}\frac{\partial T}{\partial t}, \tag{S18}$$

where q is the body heat flux due to Joule heat from the electrode, and is given by $q = \sigma\nabla\phi\cdot\nabla\phi$; σ is the electrical conductivity, and the electric potential ϕ is determined from the Maxwell equation $\nabla^2\phi = 0$ (9). The heart is modeled as a disk of radius 10 mm and thickness $h = 10\,\text{mm}$. The top surface of the heart has the boundary conditions $\phi = \phi_0$ and $-\sigma\frac{\partial\phi}{\partial z} = 0$ in and out of the region of electrode contact, respectively, where ϕ_0 is the prescribed voltage. The bottom surface has the boundary condition $\phi = 0$. The electric potential is obtained analytically as

$$\phi = \frac{2\phi_0}{\pi}\int_0^\infty \frac{\sinh\left[\xi\left(h-z\right)\right]}{\xi\sinh\left(\xi h\right)}\sin\left(\xi R_0\right)J_0\left(\xi r\right)\mathrm{d}\xi\,, \tag{S19}$$

where R_0 is the radius of electrode contact. The temperature field, when the electrode contacts the heart, is then obtained analytically as

$$T = T_\infty + \sigma\int_0^\infty\int_0^h \nabla\phi\left(r',z'\right)\cdot\nabla\phi\left(r',z'\right)G\left(r,z\middle|r',z';t\right)\mathrm{d}r'\mathrm{d}z'\,, \tag{S20}$$

where

$$G\left(r,z\middle|r',z';t\right)=\frac{2\alpha}{kh}\sum_{n=0}^{\infty}\cos\left(\frac{n\pi z}{h}\right)\cos\left(\frac{n\pi z'}{h}\right)\int_0^{\infty}\frac{J_0\left(\xi r'\right)r'}{\kappa_{2n}}\left(1-\mathrm{e}^{-\kappa_{2n}t}\right)J_0\left(\xi r\right)\xi\mathrm{d}\xi \quad \text{(S21)}$$

and $\kappa_{2n}=\alpha\left(\xi^2+\frac{n^2\pi^2}{h^2}\right)$, and J_0 is zeroth order Bessel function of the first kind. The temperature is also obtained analytically after the electrode is removed.

Figure S6*A* shows the temperature variation at r =4 mm obtained by the numerical method, which agrees well with the experimental results of the #2 sensor. The spatial distribution of the temperature in Fig. S6*B*, at the time $t_0=33\,\mathrm{s}$ when the probe is removed, suggests the lesion size ~4.4 mm, and lesion depth ~3.7 mm for a critical lesion temperature of ~70 $^{\mathrm{o}}$C.

9. Mechanics of the strain gauge

The strain in the gauge is obtained analytically by superposition method depicted in Fig. S12*A*. The strain in the middle frame of Fig. S12*A* is $\varepsilon_1=\varepsilon_a$, and the strain in the bottom frame of Fig. S12*A* could be solved by assuming interfacial shear stress distribution of $\tau=kx^3$ at the bottom of the gauge ($-kx^3$ on the top of the substrate) as shown in Fig. S12*B*. The gauge is modelled as a beam with cross section (surface normal in the x-direction) of Fig. S12*C*. The displacement of the gauge is solved by the equilibrium of the beam. The substrate is modelled as a semi-infinite space because its thickness is ~100 times larger than that of the gauge. The displacement of the substrate (silicone) at ($x=L_g/2$, $y=z=0$), is

obtained by integration of the Mindlin solution for a point force over the interface of $w_g \times L_g$, i.e.

$$u_{sub} = -\frac{1+\nu_{silicone}}{\pi E_{silicone}} \int_{-w_g/2}^{w_g/2} \int_{-L_g/2}^{L_g/2} \left\{ \frac{1-\nu}{\sqrt{\left(\frac{L_g}{2}-X\right)^2+Y^2}} + \frac{\nu\left(\frac{L_g}{2}-X\right)^2}{\left[\left(\frac{L_g}{2}-X\right)^2+Y^2\right]^{3/2}} \right\} kX^3 dXdY \quad ,(S12)$$

$$= \frac{-kL_g^3 w_g}{32\pi E_{silicone}} g_2\left(\frac{w_g}{L_g}, \nu_{silicone}\right)$$

where

$$g_2 = 2\left(1+\nu_{silicone}\right)\left[2-\left(1+2\nu_{silicone}\right)\frac{w_g^2}{L_g^2}\right]\ln\left(\frac{\sqrt{L_g^2+w_g^2}+2L_g}{w_g}\right)$$

$$-2\left(1+\nu_{silicone}\right)\left(3+5\nu_{silicone}\right)\sqrt{4+\frac{w_g^2}{L_g^2}} \quad . \quad (S13)$$

$$-\frac{2}{3}\left(1+\nu_{silicone}\right)\left(1+3\nu_{silicone}\right)\left[\frac{w_g^3}{L_g^3}-\left(\sqrt{4+\frac{w_g^2}{L_g^2}}\right)^3\right]+\frac{6w_g}{L_g}\left(1+\nu_{silicone}\right)^2$$

Compatibility requires the u_{sub} equal to the shortening of the gauge, which gives k analytically, and therefore the strain in the gauge ε_2. The strain on the top frame of Fig. S12*A* is $\varepsilon = \varepsilon_1 + \varepsilon_2$, and its average over the length L_g, $\left(1/L_g\right)\int_{-L_g/2}^{L_g/2} \varepsilon dx$, is obtained analytically as

$$\varepsilon_g = \frac{\varepsilon_a}{1+\frac{5(EA)_g}{\pi E_{silicone} L_g^2} g_2\left(\frac{w_g}{L_g}, \nu_{silicone}\right)} . \quad (S14)$$

The effective gauge factor is then given as Eq. (4) in the text.

The same idea is applied to calculate the energy release rate between the silicone substrate and the tissue (e.g. chicken breast, epicardial surface). Since the small, stiff gauges do not alter the mechanical behavior of the silicone (see text), the total energy U_{tot} of the system consists of the membrane energy of the silicone and the elastic energy of the tissue, and is obtained analytically as:

$$U_{tot}=\frac{\varepsilon_a^2\left(EA\right)_{silicone}L}{1+\frac{5\left(EA\right)_{silicone}}{\pi E_{tissue}L^2}g_2\left(\frac{w_{silicone}}{L},\nu_{tissue}\right)}\left[1-\frac{10}{9}\frac{1}{1+\frac{5\left(EA\right)_{silicone}}{\pi E_{tissue}L^2}g_2\left(\frac{w_{silicone}}{L},\nu_{tissue}\right)}\right] \quad \text{(S15)}$$

where $(EA)_{silicone}$ and $w_{silicone}$ are the tensile stiffness and width of the silicone, respectively; E_{tissue} and ν_{tissue} are the Young's modulus and Poisson's ratio of the tissue, respectively; $L=L_{silicone}-2c$ is the bonded length between the silicone and the tissue, with $L_{silicone}$ being the total length of the silicone and c the assumed crack length at the edge of the silicone. And the energy release rate is given by $G=-\left(1/2\right)\left(\partial U_{tot}/\partial c\right)\big|_{L=L_{silicone}}=\left(\partial U_{tot}/\partial L\right)\big|_{L=L_{silicone}}$. Using experimental data of ε_a=20%, $(EA)_{silicone}$=0.42 N, $L_{silicone}$=14 mm, $w_{silicone}$=7.0 mm, ν_{tissue}~0.45, E_{tissue}=40 kPa, this model gives G=8.0 mN/m which is ~250 times smaller than the interfacial work of adhesion between the two layers (~0.2 N/m,). To validate surface adhesion, we performed *in vitro* tests by laminating the silicone-supported stretchable strain gauges on the surface of a chicken breast, as shown in the left frame of Fig. S13*A*. When the chicken breast is stretched uniaxially by 20%, Fig. S13*B* right frame shows the gauge factor measured in this condition (0.25) is almost the same as that measured on a

freestanding gauge (0.23), indicating that deformation in the chicken breast is indeed fully transferred to the soft gauge through interfacial shear stress. Figure S13*C* confirms that there is no sliding between the tissue and the gauge even after the chicken breast is stretched beyond its failure strain (20%). This observation is consistent with the above modelling results which show the energy release rate being much smaller than the interfacial work of adhesion.

FEA results (Fig. S12*D*) also indicate that the gauge only reduces the strain in a thin layer (~20% of the substrate thickness) of the silicone substrate underneath it; the strain averaged throughout the depth of the silicone in this region is 8.0% for an applied strain of 10%. Therefore, the huge elastic mismatch between the silicon NM resistor and the substrate does not alter the overall mechanical behavior of the silicone substrate, which is acting as a strain isolation layer between the tissue and the stiff silicon NM (50, 51). The devices exhibit highly reproducible behavior under cyclical loads with strains of ~30% (Fig. S8*B*). We note that bending deformations can also affect the response, as quantified by measuring the response due to wrapped around cylinders with various radii (Fig. S13*A*).

10. Mechanical stress on webs during balloon inflation/deflation cycles

The web designs minimize strains in the sensory elements of balloon systems, and thereby enhance durability during inflation and deflation of the balloon support. Compressive strains in the circuits reach maximum levels when the balloon is totally deflated. At this stage, the balloon folds into uniform ‘clover’ patterns (cross-section of

Fig. 4*B* and Fig. S14, left) driven by the pressure mismatch inside (~vacuum) and outside of the balloon (p_{air} ~1 atm). The deformed profile of each clover-fold can be obtained analytically, and verified using FEA (Fig. S14, right). The maximum curvature occurs at the peaks of the folds, and is given by $\kappa_{\max} = 2.1\left(p_{\text{air}} / \overline{EI}_{\text{balloon}} \right)^{1/3}$, where $\overline{EI}_{\text{balloon}}$ is the bending stiffness of the balloon with circuits. The strain in the circuits/balloon membrane is then obtained as

$$\varepsilon_{\max} = \kappa_{\max} y, \tag{S16}$$

where y is the distance from the neutral mechanical plane (Fig. S10). This result gives the maximum strain 0.31% in gold and 1.7% in polyimide, which are much smaller than the strains 28.7% in the adhesive (encapsulation) and 39.5% polyurethane (balloon membrane) layers. The compliant photo-curable adhesive (Dymax Inc.) and polyurethane accommodate large deformation resulting from deflation, such that the strains in active components are small. The minimal curvature regions (κ=0, Fig. S14, right) undergo minimal deformation during deflation, and therefore represent the optimal locations for selective positioning of devices. These modeling results also represent a framework for integrating conformal sensors on various classes of collapsible balloons, beyond those described in this study.

SI References

1. Kim D*, et al* (2011) Epidermal electronics. *Science* 333: 838-843.

2. Wang S, *et al* (2011) Mechanics of epidermal electronics. *J Appl Mech* 79:3, article 031022.

3. Lu N, Yoon J & Suo Z (2007) Delamination of stiff islands patterned on stretchable substrates. *Int J Mater Res* 98: 717-722.

4. Barber JR (2010) in *Elasticity* (Springer, Dordrecht 3rd edn), pp 363-374.

5. Patronik NA, Ota T, Zenati MA & Riviere CN (2006) Improved traction for a mobile robot traveling on the heart. *Engineering in Medicine and Biology Society, 2006 28th Annual International Conference of the IEEE*: 339-342.

6. Martin RW & Johnson CC (1989) Design characteristics for intravascular ultrasonic catheters. *Int J Cardiac Imag* 4: 201-216.

7. Dhir V, Castle J & Catton I (1977) Role of taylor instability on sublimation of a horizontal slab of dry ice. *J Heat Trans-T ASME* 99: 411-418.

8. Consiglieri L, dos Santos I & Haemmerich D (2003) Theoretical analysis of the heat convection coefficient in large vessels and the significance for thermal ablative therapies. *Phys Med Biol* 48: 4125-4134.

9. Berjano EJ (2006) Theoretical modeling for radiofrequency ablation: State-of-the-art and challenges for the future. *Biomed Eng Online* 5: 24.

SI Figure Legends

Figure S1. (*A*) Layout of an electrode web. (*B*) A magnified view of one pair of electrodes, corresponding to the red dotted box in Fig. S1*A*. (*C*) Cross-sectional diagram of the array. (*D*) Schematic illustration of fabrication and deployment of a cardiac mapping web.

Figure S2. Analytical modelling of serpentine interconnects: (*A*) Geometry of double serpentine interconnects in the *y*-direction. (*B*) Geometry of single serpentine interconnect in the *x*-direction. (*C*) Representative cell of the mapping electrode arrays. (*D*) strain distribution in the polyimide layer of circuits under 10% stretching in both *x*- and *y*-directions. (*E*) Strain distribution in the gold layer of circuits under 10% stretching in both *x*- and *y*- directions. (*F*) Coordinate system for obtaining the displacement of an electrode island (grey) bonded on the surface of the heart (red).

Figure S3. (*A*) Layout of stretchable temperature sensors. (*B*) A magnified view of one pair of electrode design, which corresponds to red dotted box in Fig. S3*A*. (*C*) Cross-sectional diagram of the array.

Figure S4. (*A*) Schematic diagram of leakage current circuitry showing resistor (R_1) in series with R_2, denoting the leakage current escaping and passing through the saline to ground. Leakage current was monitored by measuring voltages across R_1. (*B*) Drawing shows the contact sensor (device under test; DUT) in a bath of saline. Large amounts of leakage current existed in the case where the voltage across R1 approached the input

voltage. Leakage currents were controlled with an isolated power supply to prevent leakage currents from entering the body.

Figure S5. (*A*) Axisymmetric heat conduction model for cryoablation. (*B*) Temperature distribution from the modelling (solid lines) agrees well with experimental measurements (square dots).

Figure S6. (*A*) Temperature recorded during RF ablation. The location of the temperature sensor is at position #2. (*B*) The 3D temperature distribution around the RF probe suggests a lesion size of 4.4 mm and depth of 3.7 mm.

Figure S7. (*A*) Layout of a strain gauge web. (*B*) A magnified view the design, corresponding to the red dotted box in Fig. S7*A*. (*C*) Cross-sectional diagram of the array.

Figure S8. (*A*) Change of resistance as a function of uniaxial tensile strain for longitudinal, diagonal and transverse resistors. The gauge factor of the longitudinal resistor is 0.23. *(B)* Response of a longitudinal strain gauge under cyclic uniaxial stretching up to 30%.

Figure S9. (*A*) Schematic drawing of *in vitro* testing with impedance-based contact sensors placed in contact with raw chicken breast meat. (*B*) The results highlight differences detected with contact sensors on wet tissue versus saline.

Figure S10. Material and geometric properties of the contact sensor web device for mounting on a balloon catheter.

Figure S11. (*A*) Circuit diagram of 16-channel contact sensing array. Voltages were measured across the same two terminals where constant current was applied (1-100 kHz). (*B*,*C*) Photographs of National Instruments data acquisition system with impedance analysis hardware (red circle) and control software running in Labview.

Figure S12. (*A*) Superposition method to obtain the strain in the gauge. (*B*) Interfacial shear stress between the gauge and the substrate for the problem in the bottom frame of Fig. S12*A*. (*C*) Cross-sectional diagram of the gauge (PI in golden and silicon in grey). (*D*) Strain distribution under the Si NM strain gauge for applied strain of 10%.

Figure S13. (*A*) Bending tests of the strain gauges. (*B*) Strain gauge web laminated on raw chicken breast meat under uniaxial tension. (*C*) *In vitro* stretching experiment on chicken. No slippage occurred as the applied strain increased up to ~20%.

Figure S14. End-on view of a device in its deflated state (left) and corresponding schematic cross-sectional illustration (middle). The deformed shape under deflation obtained by both analytical modeling and FEA (right).

Supporting Information Table S1

	Tensile stiffness (N/m)	Theory	FEA
Without silk	x-direction	17.6	16.9
	y-direction	15.0	14.7
With silk	x-direction	7.0E4	7.0E4
	y-direction	7.0E4	6.9E4

Table S1 Comparison between analytical and FEA results for tensile stiffness

Supporting Information Table S2

	Bending stiffness (N-m)	Theory	FEA
Without silk	x-direction	3.7E-10	3.2E-10
	y-direction	2.8E-10	2.7E-10
With silk	x-direction	4.3E-6	4.7E-6
	y-direction	4.3E-6	4.8E-6

Table S2 Comparison between analytical and FEA results for bending stiffness

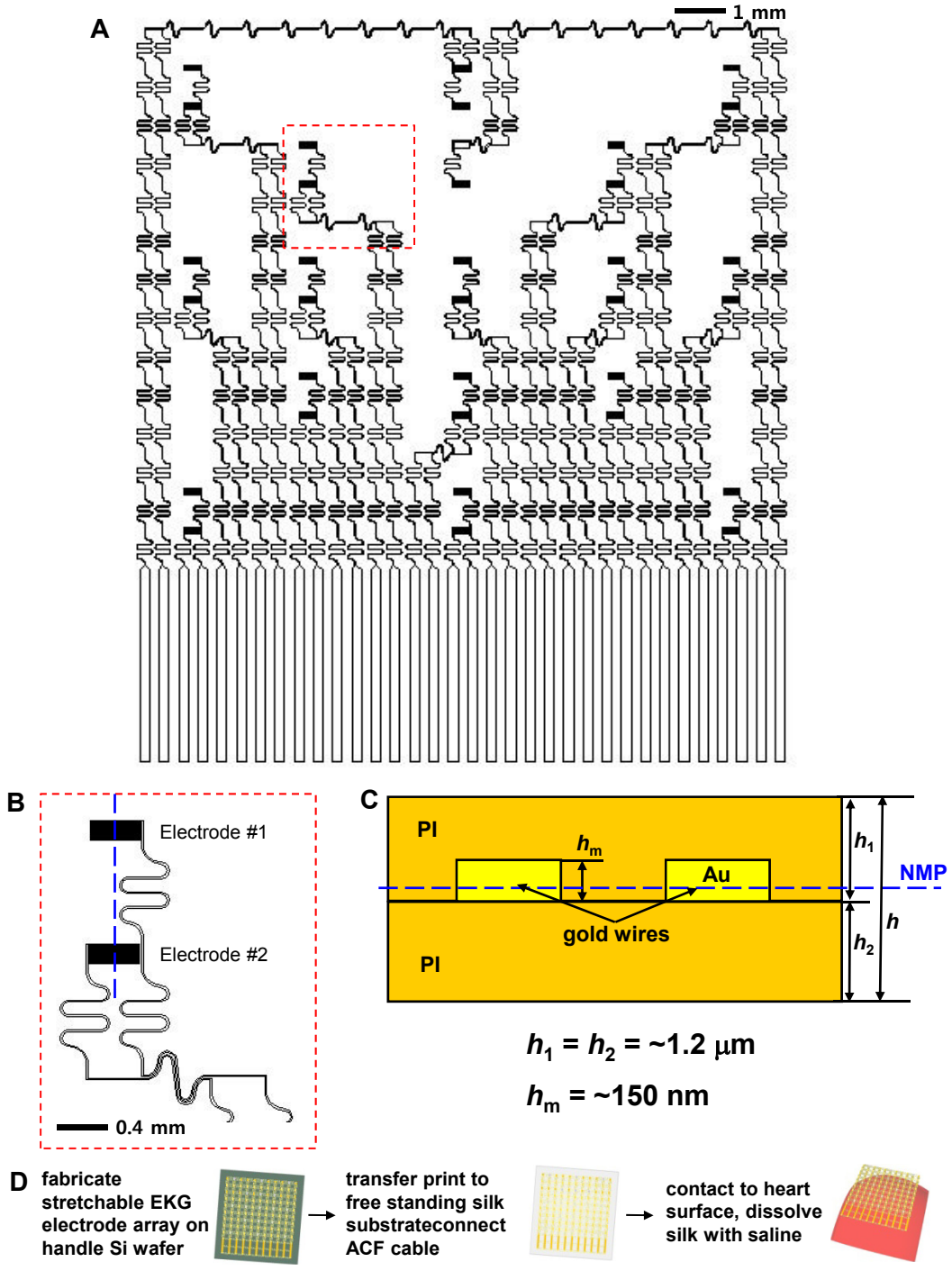
A
1 mm
B
Electrode #1
Electrode #2
0.4 mm
C
PI
h_m
Au
h_1
NMP
gold wires
h
h_2
PI
$h_1 = h_2 = \sim 1.2\ \mu m$
$h_m = \sim 150\ nm$
D
fabricate stretchable EKG electrode array on handle Si wafer
transfer print to free standing silk substrateconnect ACF cable
contact to heart surface, dissolve silk with saline

Figure S1

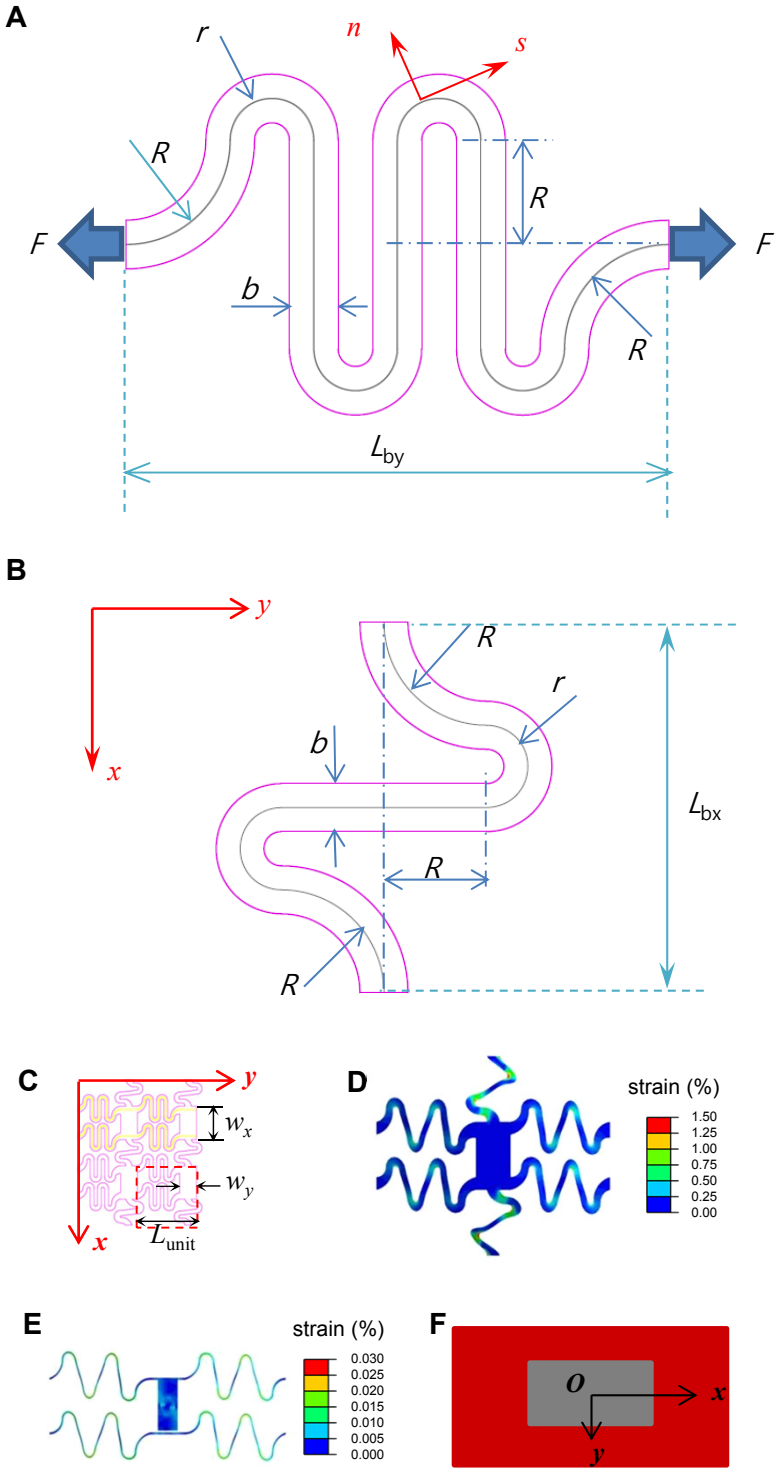
A
r
n
s
R
R
F
F
b
R
L_{by}
B
y
x
R
r
b
R
R
L_{bx}
C
y
x
w_x
w_y
L_{unit}
D
strain (%)
1.50
1.25
1.00
0.75
0.50
0.25
0.00
E
strain (%)
0.030
0.025
0.020
0.015
0.010
0.005
0.000
F
o
x
y

Figure S2

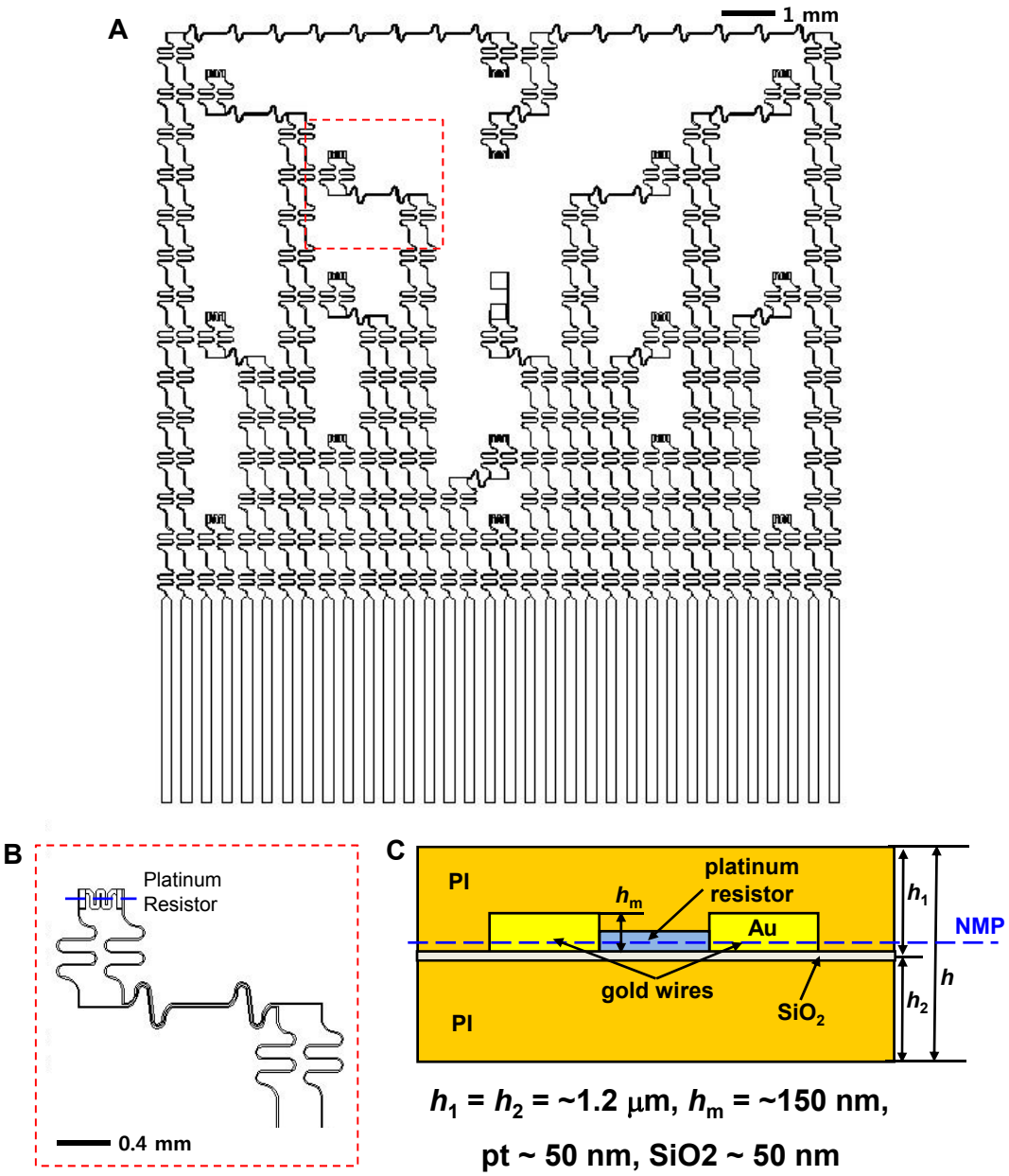
A
1 mm
B
Platinum
Resistor
0.4 mm
C
PI
platinum
resistor
h_m
Au
NMP
h_1
h_2
h
gold wires
SiO_2
PI
$h_1 = h_2$ = ~1.2 μm, h_m = ~150 nm,
pt ~ 50 nm, SiO2 ~ 50 nm

Figure S3

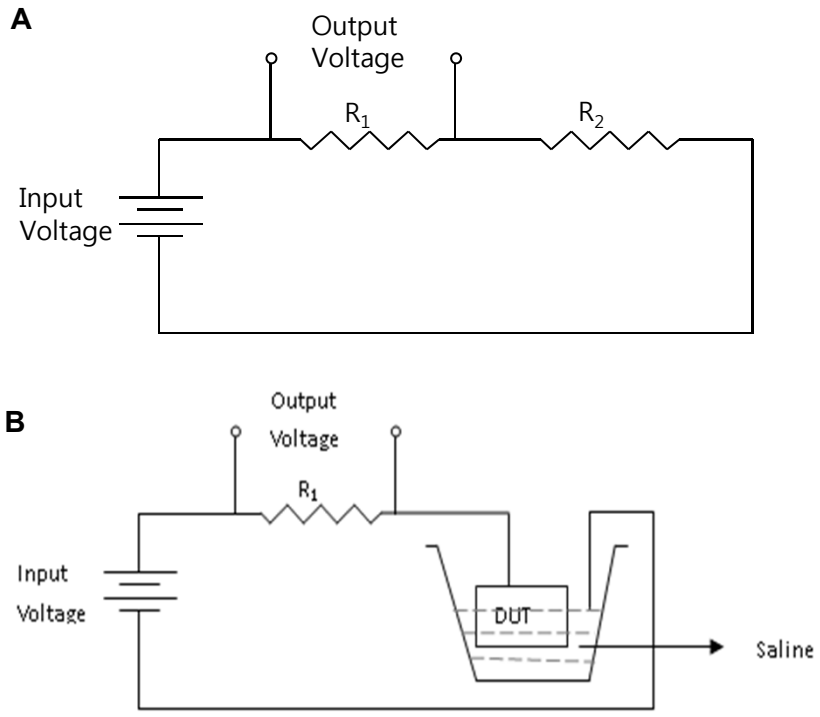
A
Output
Voltage
R1
R2
Input
Voltage
B
Output
Voltage
R1
Input
Voltage
DUT
Saline

Figure S4

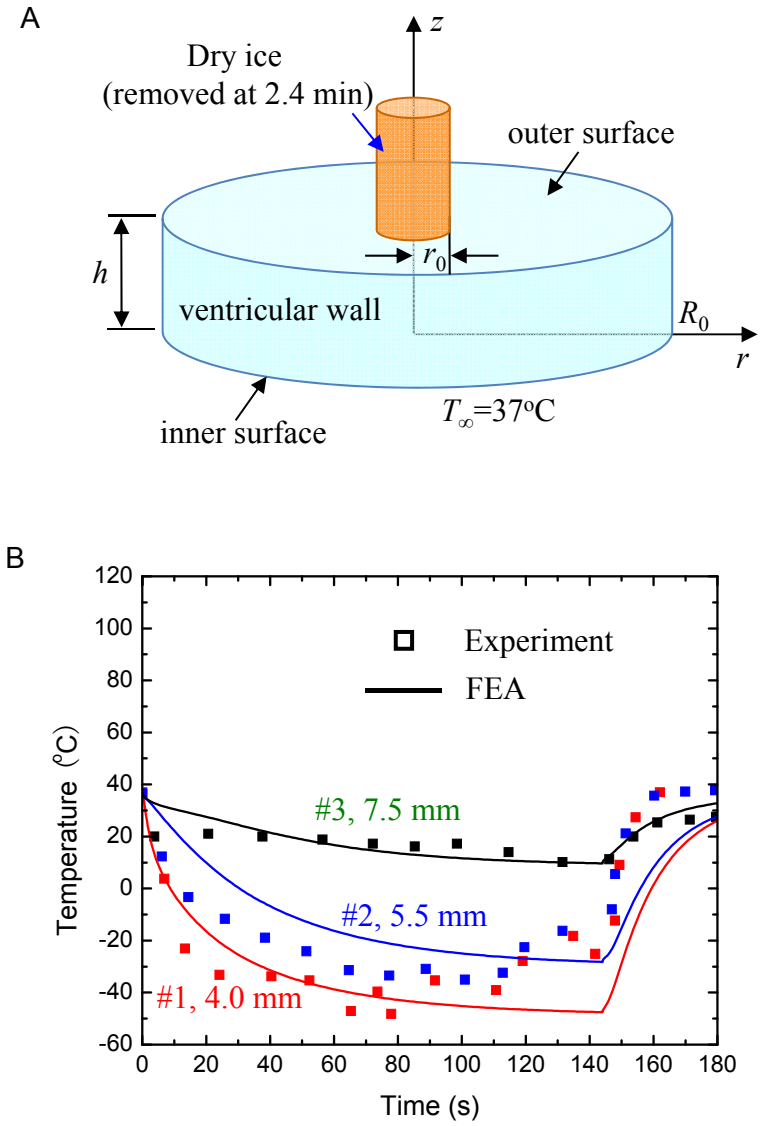
A
z
Dry ice
(removed at 2.4 min)
outer surface
h
r_0
ventricular wall
R_0
r
inner surface
T_∞=37°C
B
Experiment
FEA
#3, 7.5 mm
#2, 5.5 mm
#1, 4.0 mm
Temperature (°C)
Time (s)
120
100
80
60
40
20
0
-20
-40
-60
0
20
40
60
80
100
120
140
160
180

Figure S5

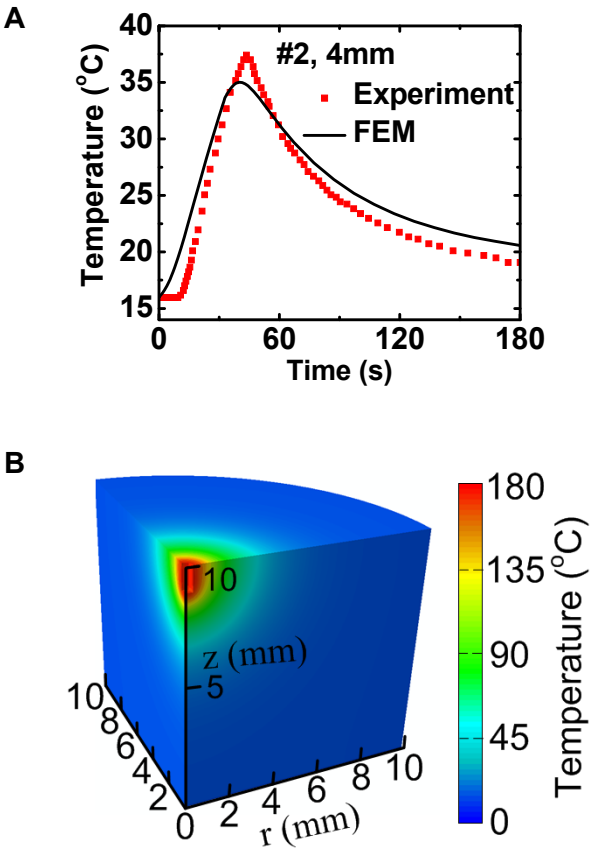
A
Temperature (°C)
40
35
30
25
20
15
0
60
120
180
Time (s)
#2, 4mm
Experiment
FEM
B
10
z (mm)
5
10
8
6
4
2
0
2
4
6
8
10
r (mm)
180
135
90
45
0
Temperature (°C)

Figure S6

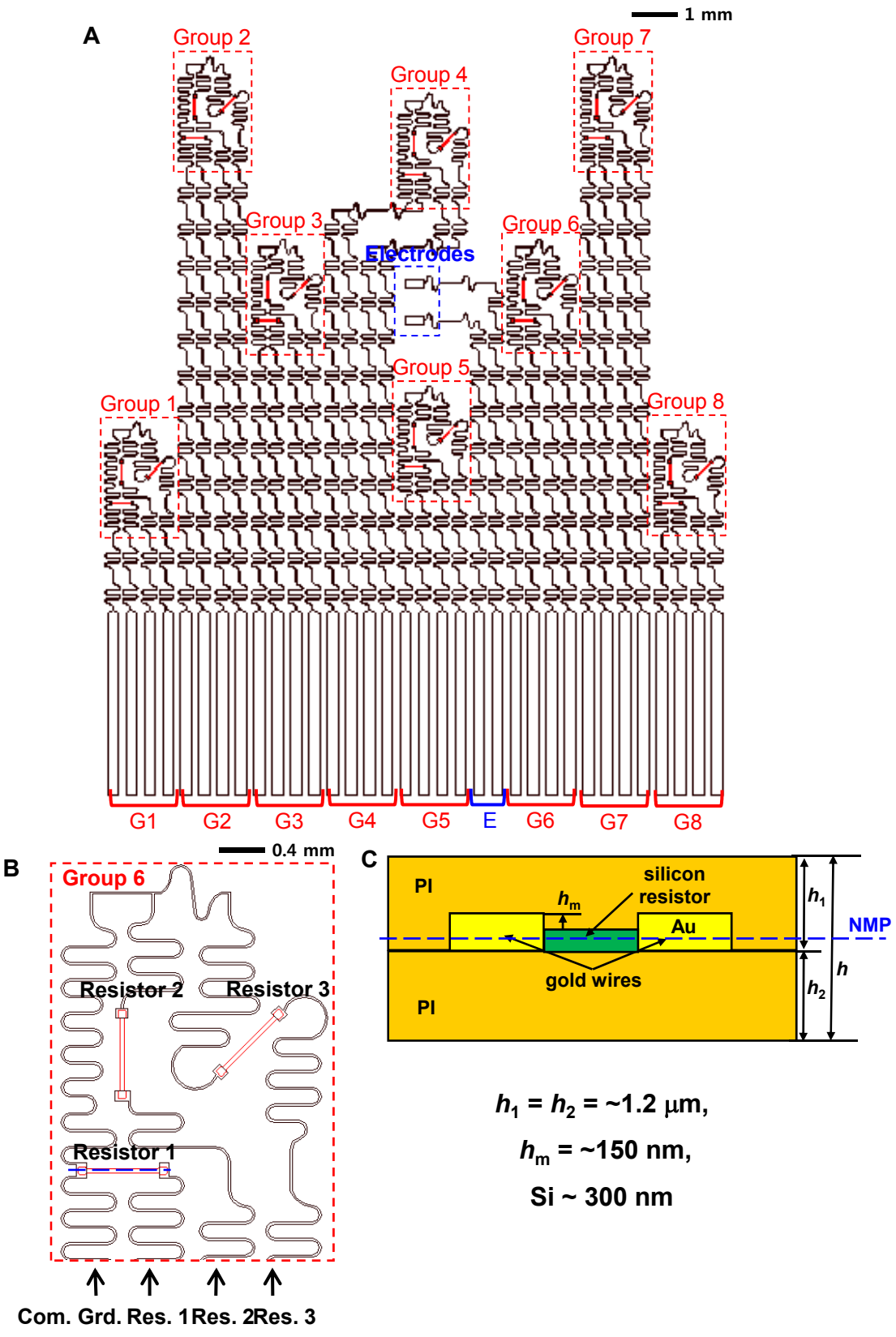
A
1 mm
Group 2
Group 4
Group 7
Group 3
Electrodes
Group 6
Group 5
Group 1
Group 8
G1
G2
G3
G4
G5
E
G6
G7
G8
B
0.4 mm
Group 6
Resistor 2
Resistor 3
Resistor 1
Com.
Grd.
Res. 1
Res. 2
Res. 3
C
PI
silicon resistor
h_m
Au
h_1
NMP
gold wires
h
h_2
PI
h_1 = h_2 = ~1.2 μm,
h_m = ~150 nm,
Si ~ 300 nm

Figure S7

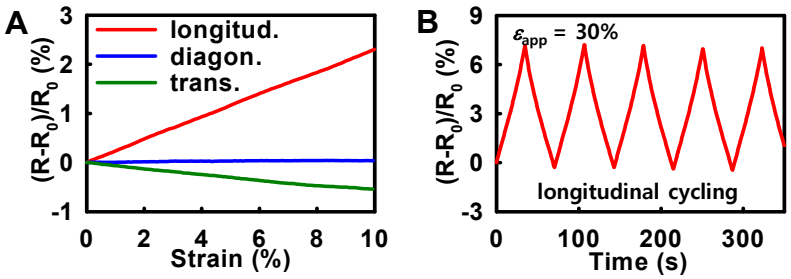
A
longitud.
diagon.
trans.
(R-R0)/R0 (%)
Strain (%)
B
εapp = 30%
longitudinal cycling
(R-R0)/R0 (%)
Time (s)

Figure S8

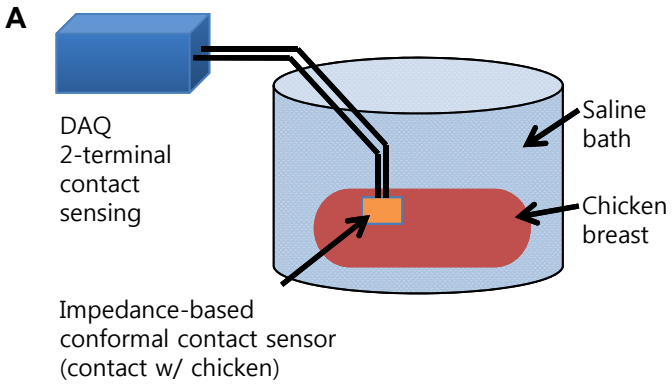
A
DAQ
2-terminal
contact
sensing
Saline
bath
Chicken
breast
Impedance-based
conformal contact sensor
(contact w/ chicken)

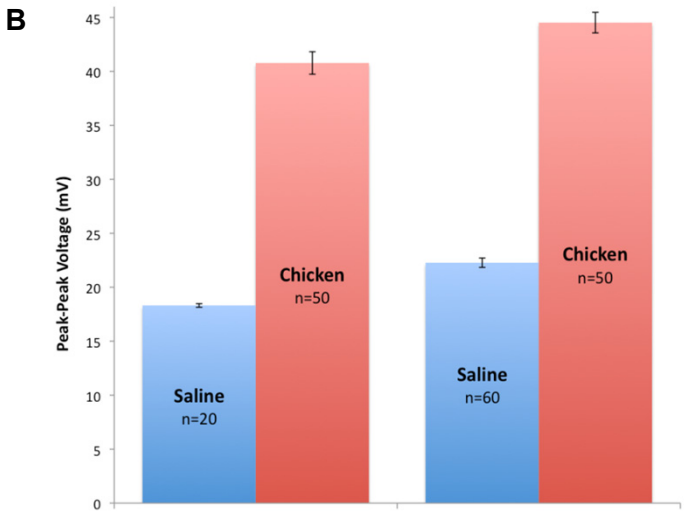
B
Peak-Peak Voltage (mV)
45
40
35
30
25
20
15
10
5
0
Saline
n=20
Chicken
n=50
Saline
n=60
Chicken
n=50

Figure S9

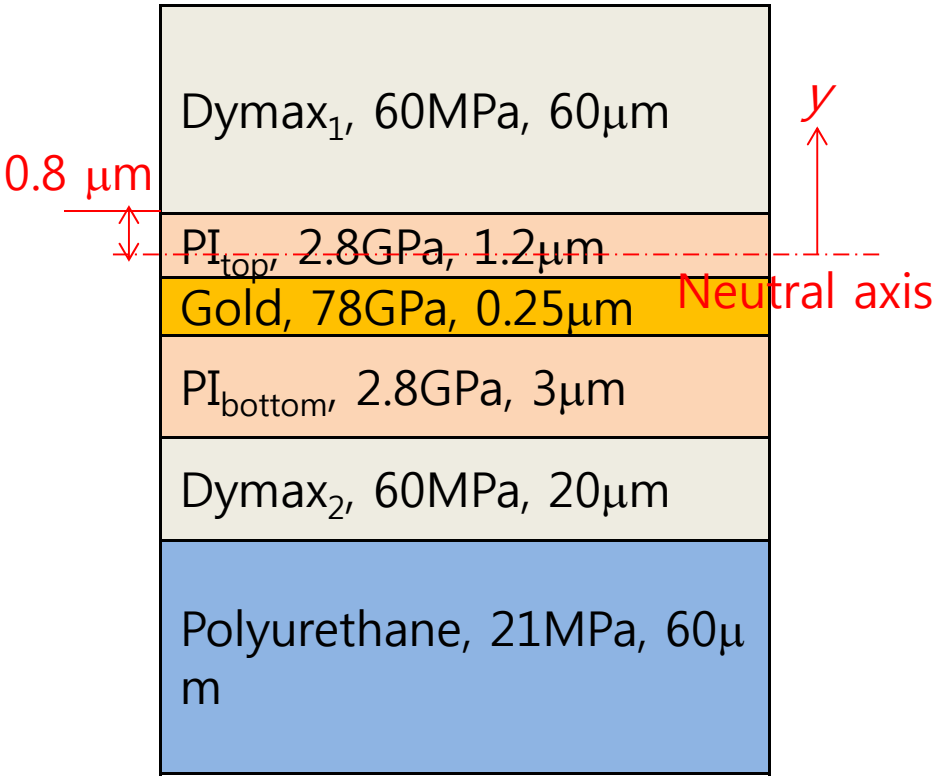
Dymax1, 60MPa, 60μm
0.8 μm
PItop, 2.8GPa, 1.2μm
Gold, 78GPa, 0.25μm
PIbottom, 2.8GPa, 3μm
Dymax2, 60MPa, 20μm
Polyurethane, 21MPa, 60μm
y
Neutral axis

Figure S10

A

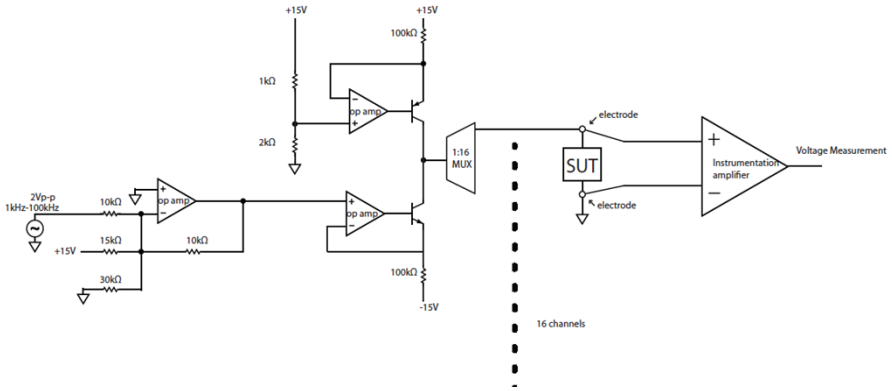

B

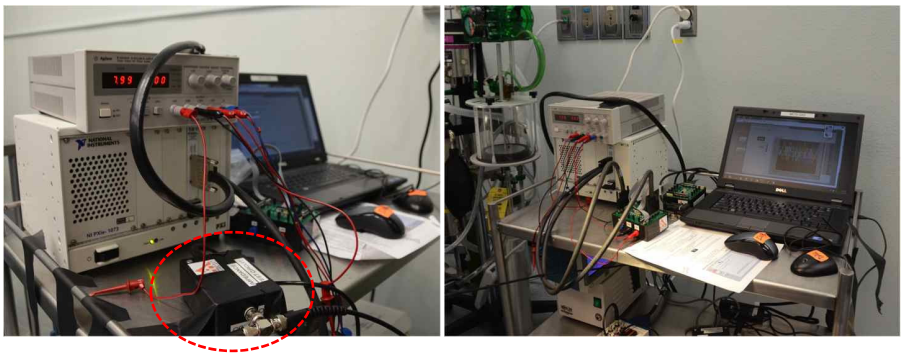

- Custom National Instruments data acquisition system (NI PXI-6289)
- Impedance analysis at 1 kHz, 10 kHz, 100 kHz
- Control software in LABVIEW
- Single-channel analog inputs, 18-bits

Figure S11

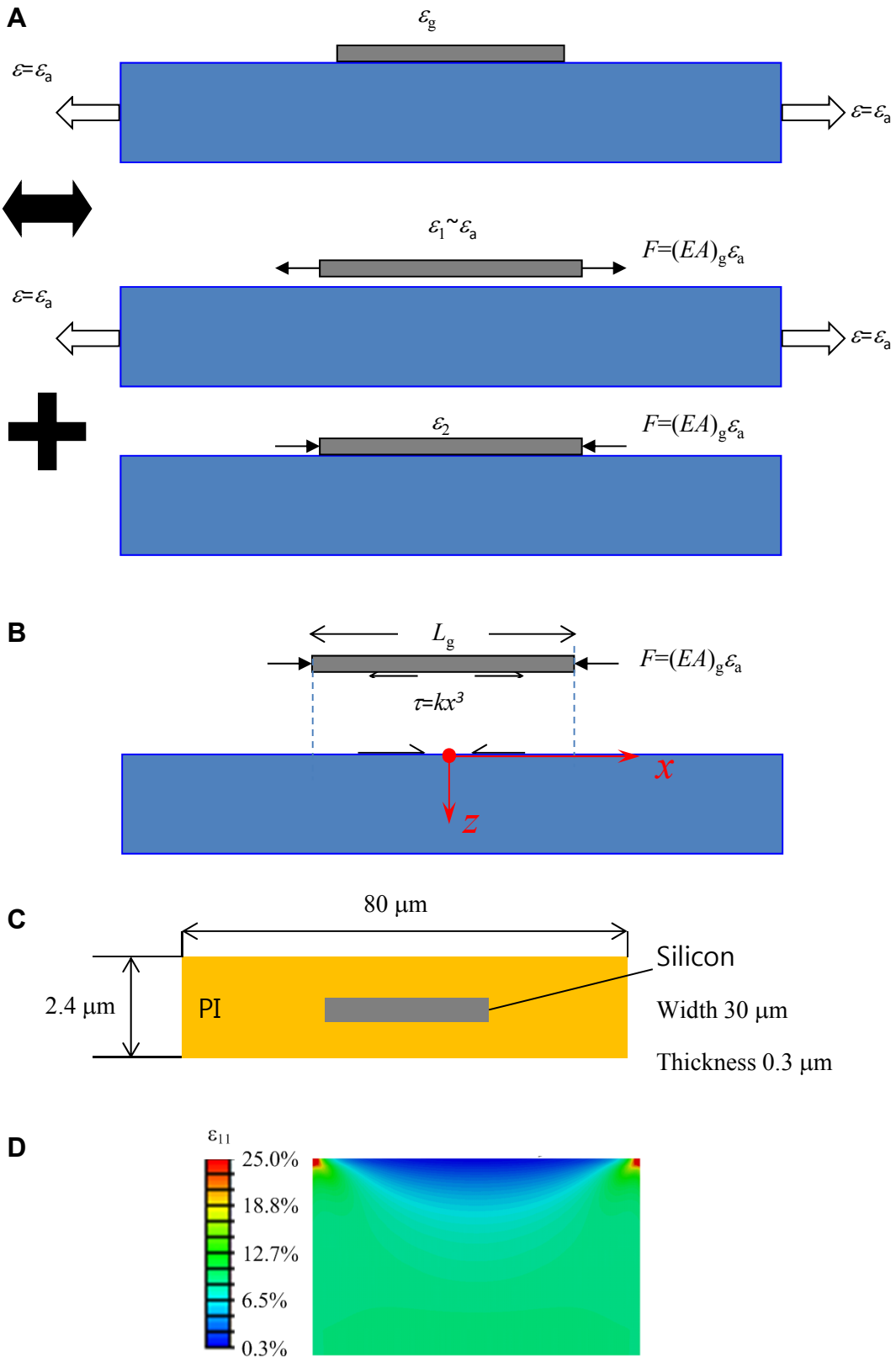
A
ε_g
$\varepsilon=\varepsilon_a$
$\varepsilon=\varepsilon_a$
$\varepsilon_1 \sim \varepsilon_a$
$F=(EA)_g\varepsilon_a$
$\varepsilon=\varepsilon_a$
$\varepsilon=\varepsilon_a$
ε_2
$F=(EA)_g\varepsilon_a$
B
L_g
$F=(EA)_g\varepsilon_a$
$\tau=kx^3$
x
z
C
80 μm
2.4 μm
PI
Silicon
Width 30 μm
Thickness 0.3 μm
D
ε_{11}
25.0%
18.8%
12.7%
6.5%
0.3%

Figure S12

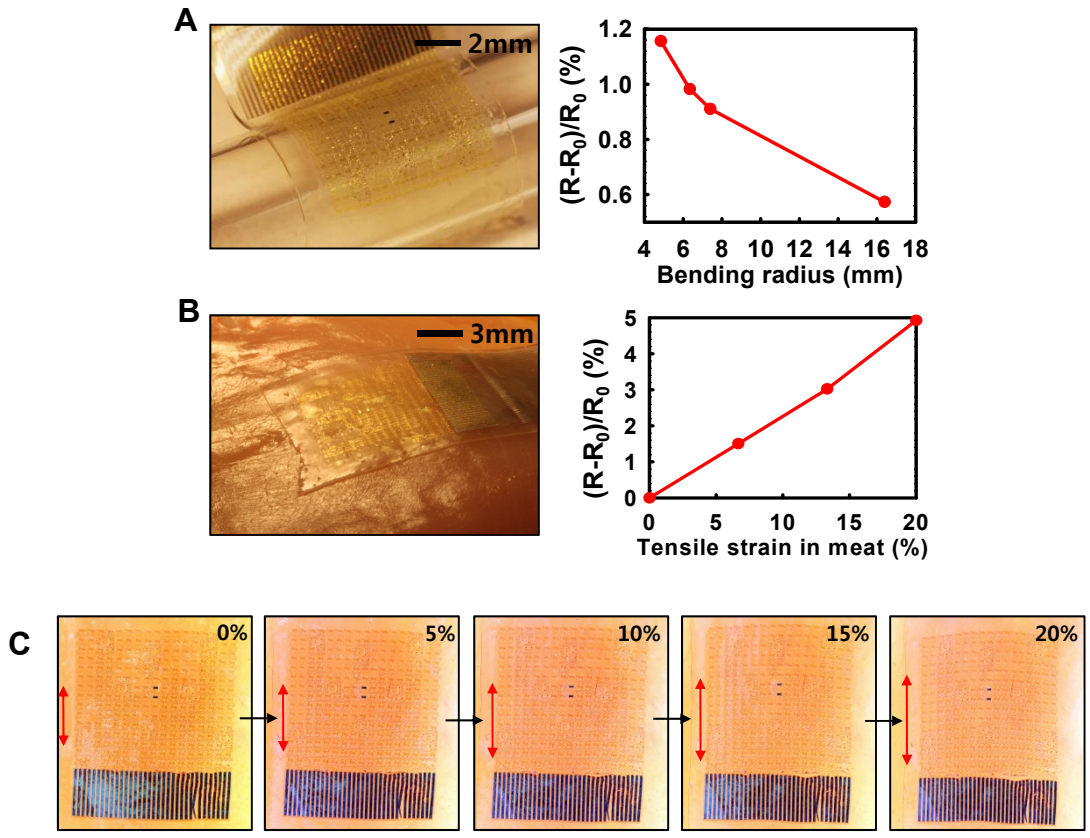
A
2mm
1.2
1.0
0.8
0.6
(R-R0)/R0 (%)
4 6 8 10 12 14 16 18
Bending radius (mm)
B
3mm
5
4
3
2
1
0
(R-R0)/R0 (%)
0 5 10 15 20
Tensile strain in meat (%)
C
0%
5%
10%
15%
20%

Figure S13

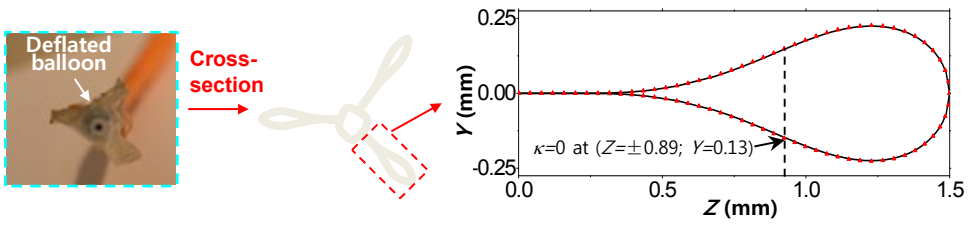
Deflated balloon
Cross-section
0.25
0.00
-0.25
Y (mm)
κ=0 at (Z=±0.89; Y=0.13)
0.0
0.5
1.0
1.5
Z (mm)

Figure S14